 MCB, vol.4, no.2, pp.87-104, 2007

Geometric Confinement Influences Cellular Mechanical Properties I – Adhesion Area Dependence

Judith Su*, Xingyu Jiang†, Roy Welsch‡, George M. Whitesides§, Peter T. C. So¶

Abstract: Interactions between the cell and the extracellular matrix regulate a variety of cellular properties and functions, including cellular rheology. In the present study of cellular adhesion, area was controlled by confining NIH 3T3 fibroblast cells to circular micropatterned islands of defined size. The shear moduli of cells adhering to islands of well defined geometry, as measured by magnetic microrheometry, was found to have a significantly lower variance than those of cells allowed to spread on unpatterned surfaces. We observe that the area of cellular adhesion influences shear modulus. Rheological measurements further indicate that cellular shear modulus is a biphasic function of cellular adhesion area with stiffness decreasing to a minimum value for intermediate areas of adhesion, and then increasing for cells on larger patterns. We propose a simple hypothesis: that the area of adhesion affects cellular rheological properties by regulating the structure of the actin cytoskeleton. To test this hypothesis, we quantified the volume fraction of polymerized actin in the cytosol by staining with fluorescent phalloidin and imaging using quantitative 3D microscopy. The polymerized actin volume fraction exhibited a similar biphasic dependence on adhesion area. Within the limits of our simplifying hypothesis, our experimental results permit an evaluation of the ability of established, micromechanical models to predict the cellular shear modulus based on polymerized actin volume fraction. We investigated the "tensegrity", "cellular-solids", and "biopolymer physics" models that have, respectively, a linear, quadratic, and 5/2 dependence on polymerized actin volume fraction. All three models predict that a biphasic trend in polymerized actin volume fraction as a function of adhesion area will result in a biphasic behavior in shear modulus. Our data favors a higher-order dependence on polymerized actin volume fraction. Increasingly better experimental agreement is observed for the tensegrity, the cellular solids, and the biopolymer models respectively. Alternatively if we postulate the existence of a critical actin volume fraction below which the shear modulus vanishes, the experimental data can be equivalently described by a model with an almost linear dependence on polymerized actin volume fraction; this observation supports a tensegrity model with a critical actin volume fraction.

Keyword: magnetic trap; microcontact printing; cytoskeleton; mechanotransduction

1 Introduction

The cytoskeleton – the primary structural component of the cell – determines the mechanical response of the cell to an externally applied load (1). The cytoskeleton plays a major role in cellular processes such as migration, mitosis, and adhesion (1). Changes in cellular compliance can influence the expression of genes and the production of proteins, and can combine with other factors such as adhesion strength to effect cellular movement and differentiation (2). The study of cellular rheology and its molecular basis is an active area of research in biomechanics, with sev-

* Department of Mechanical Engineering, MIT. Present address: Biochemistry and Molecular Biophysics Option, Caltech.
† Department of Chemistry and Chemical Biology, Harvard University. Present address: National Center for NanoScience and Technology, China.
‡ Statistics and Management Science, MIT.
§ Department of Chemistry and Chemical Biology, Harvard University
¶ Department of Biological Engineering and Department of Mechanical Engineering, MIT.

eral fundamentally different models proposed to link macroscopic properties of the cell with microstructural detail of the cytoskeleton (1). The simplest representation of cytoskeletal mechanics approximates the cell as a continuum, and uses springs and dashpots to represent its viscoelastic behavior (3). Other structurally based models, such as the tensegrity model proposed by Ingber and co-workers, take into account how individual cytoskeletal components contribute to the elasticity of the cytoskeleton (4). A recent study by Fabry et al presents results that suggest that the cytoskeleton behaves as a soft glassy material, and imply that the cytoskeleton may deform and flow like a liquid (5).

One key accomplishment in the study of cytoskeletal mechanics has been the development of experimental methods to probe the cytoskeletal mechanics of cells. These methods include measurements of indentation performed by "cell squashing" and "poking" (6), micropipette aspiration (7), magnetic twisting cytometry (5), laser tracking microrheology (8), atomic force microscopy (9), and laser (10) and magnetic tweezer (11, 12, 13, 14) based microrheometers. These studies, however, do not quantitatively link cellular rheology to systematic changes in molecular structure. Further, conventional measurements of cellular rheology do not take into consideration the fact that cellular properties may be affected by the interactions between cells and their substrate. Recent developments in micropatterning make it possible to examine the effects of cellular adhesion area's size and shape (15, 16). Micropatterning further allows partial control of the biochemistry and density of cellular adhesion molecules. Previous work by Whitesides and coworkers has demonstrated that the size and shape of cells influence their passage through the cell cycle and their probability of initiating apoptosis (17). Control of cellular shape through micropatterning can also regulate aspects of cellular physiology such as motility, differentiation, and the assembly of cells into tissues (18, 19, 20, 21). We seek to elucidate the effects of cellular adhesion area on cellular rheology, and to correlate these mechanical changes with molecular level remodeling of the cytoskeleton.

Previous studies of rheological properties as a function of the characteristics describing the adhesion of the cell to the substrate involve determining the effect of fibronectin density in hepatocytes on cellular shear modulus using atomic force microscopy (22); endothelial cells have also been examined using magnetic twisting cytometry (23). These studies, however, have been unable to separate the effects of total cell area from the effect of the density of the adhesion molecule in the adhesion area. Micropatterning in combination with magnetic microrheometry allows us to quantify – precisely and systematically – cellular rheological properties and cytoskeletal structure as a function of adhesion area. This technique has allowed us to establish that the cellular shear modulus is a biphasic function of cellular adhesion area. As a rationalization of this biphasic behavior, we assume that cellular rheology is dominated by the mechanical properties of the polymerized actin network. With this simplifying assumption, standard cytoskeletal microstructural models (tensegrity, cellular solids, and biopolymer physics) predict a power law dependence of cellular shear modulus on the volume fraction of polymerized actin (defined as the ratio of the cellular volume occupied by the polymerized actin to the total cell volume). We can therefore advance the hypothesis that changes in cellular shear modulus are a direct function of the polymerized volume fraction of actin; this fraction is regulated, in turn, by the adhesion area of the cell. To test this hypothesis, we measured the volume fraction of polymerized actin as a function of area of adhesion of the cell to the substrate using phalloidin labeling and spinning disk confocal microscopy. The cellular shear modulus can be calculated based on polymerized actin volume fraction using the microstructural mechanical models. The accuracies of the shear moduli derived from the tensegrity, cellular-solids, and biopolymer physics models can then be compared with experimental magnetic microrheometry measurements.

2 Materials and Methods

2.1 Substrate preparation

Micropatterned substrates were created following the method of Whitesides and coworkers (24). A 130 Å-thick layer of gold was deposited on the coverslip bottoms of Bioptechs culture dishes (Bioptechs, Butler, PA) using electron-beam vapor deposition. To promote the adhesion of the gold to glass, 30 Å of titanium was first evaporated onto the dish. To create the polydimethylsiloxane (PDMS, Sylgard 184, Dow Corning, Midland, Michigan) stamp used for microcontact printing, negative photoresist (SU8-2015, Microchem, Newton, MA) was spin-coated for 35 seconds at 1500 rpm onto a 4" silicon wafer. The photoresist was then baked on a hotplate at 65°C for 1 minute and 95°C for 2 minutes. The photoresist was exposed to UV light for 12 seconds through a transparency photomask (Output City, Poway, CA) to create the photoresist master. Following exposure, the wafer was post-baked again at 65°C for 1 minute and 95°C for 2 minutes. The unpolymerized photoresist was washed away with propylene glycol monomethyl ether acetate (PGMEA, Microchem, Newton, MA) and the wafers were silanized for 15 minutes to prevent the PDMS from sticking. PDMS was poured on the bas relief photoresist structure and baked in an oven for 2 hours at 65°C. The PDMS stamp was then peeled off and coated with 2 mM hexadecanethiol (Sigma Aldrich, St. Louis, MO) in ethanol. Excess solvent was removed by evaporation in a stream of nitrogen, and the stamp was pressed onto the gold coverslip for 30 seconds. The stamp was then gently peeled off and the bottom of the bioptechs dish covered with 2mM of a polyethyleneglycol (PEG)-terminated alkanethiol (Prochimia, Poland) for 30 minutes. Afterwards the dishes were rinsed once with ethanol and once with phosphate buffered saline (PBS) solution, (Invitrogen Life Technologies, Carlsbad, CA).

2.2 Cell culturing and plating

Cells were cultured according to instructions provided by the American Type Culture Collection (ATCC). NIH 3T3 fibroblasts (ATCC, Manassas, VA) were grown using high glucose Dubecco's Modified Eagle Medium (DMEM) supplemented with 10% v/v bovine calf serum (Invitrogen Life Technologies, Carlsbad, CA) and 1% penicillin/streptomycin in 10 cm^2 tissue cultures plates in an incubator at 37°C until 70% confluent. Cells were split in a laminar flow hood where the media was vacuum aspirated off with a sterile pipette and 2.5 mL of trypsin-EDTA was added. The cells were placed back into the incubator for 5-7 minutes until they disassociated from the bottom of the plate. An equivalent amount of serum-containing media was added to inactivate trypsin. The solution of media and cells was gently mixed using a 5-mL pipette for several minutes until a homogeneous suspension of cells was obtained. The desired quantity of cells was added to a new tissue culture plate for continued propagation and placed back into the incubator.

To plate the cells, 0.5 mL of 0.25 μg/mL of human plasma fibronectin (Sigma Aldrich, St. Louis, MO) in PBS was placed in each stamped Bioptechs dish for four hours at 37°C. The fibronectin was aspirated out, while the desired number of cells was simultaneously pipetted. Approximately 30,000 cells were added per dish.

2.3 Actin staining

Cells were fixed with 3.7% formaldehyde (Z-fix, Anatech LTD, Battlecreek, MI) and their F-actin stained with Alexa Fluor 488-conjugated phalloidin (Molecular Probes, Eugene, Oregon) according to directions provided by Molecular Probes. The media was first aspirated and the cells were washed twice with PBS. Z-fix was added for 10 minutes and then removed by aspiration. The Bioptechs dishes were washed again twice with PBS and a solution of 0.1% Triton X-100 was added for a total of 5 minutes to allow for entry of the dye. Triton X-100 was removed and the bioptechs dishes were washed twice with PBS. The dishes were soaked then in a 1% bovine serum albumin (BSA) solution for 30 minutes to reduce non-specific binding. The staining solution consisting of 200 μL of PBS and 15 μL of methanolic dye solution was then added to each dish for 20 minutes after which the dishes were

washed again twice with PBS, once with distilled water, and gently blown dried with nitrogen.

2.4 Whole-cell stain

For total cell volume measurement, cells were incubated using a 1-μM solution of cell-tracker green (CMFDA) in media for 15 minutes at 37^{o}C. The dye-containing solution was then replaced with media for 30 minutes, after which cells were ready for imaging.

2.5 Gel and actin filament preparation

Actin (1 mg, Cytoskeleton Inc., Denver, CO) was dissolved in 100 μL of ddH_2O. General actin buffer (GAB), (Cytoskeleton Inc., Denver, CO) was added to the actin vial to create a concentration of 0.5 mg/mL. This mixture was placed on ice for one hour. Actin was polymerized by mixing 100 μL of the actin and GAB mixture with 10 μL of actin polymerizing buffer (ABP), (Cytoskeleton Inc., Denver, CO). Alexa Fluor-488 phalloidin was added at the desired concentration and this mixture was placed on ice in the dark for one hour. The solution was centrifuged for 30 minutes at 10,000 rpm to pellet the actin and wash out the excess dye. Equal volumes of filament solution were mixed with ProLong (Molecular Probes, Eugene, Oregon) on a glass slide, and the mixture left to solidify.

2.6 Magnetic bead preparation

Paramagnetic polystyrene beads (4.5 μm diameter, Dynal, Oslo, Norway) with a tosyl-activated coating were covalently conjugated to fibronectin according to instructions provided by the manufacturer. The solution containing the magnetic beads was placed on top of a magnet to draw the beads to the bottom. The storage solution was then removed by aspiration and the beads washed once in a borate buffer solution with a pH of 9.4. Fibronectin was added (5 μg/10^7 beads) and the solution was gently agitated for 10 minutes at 37^{o}C. BSA was added until its concentration was 0.1%, and the entire mixture was agitated overnight at 37^{o}C. The beads were washed three times with 0.1% BSA in PBS, and once with Tris buffer with 0.1% BSA (pH 8.5). Prior to use, the beads were mixed in 1% BSA in PBS for 5 minutes, and resuspended in media. This mixture was added to the cells 24 hours before experiments were performed.

2.7 Magnetic trap setup

The magnetic trap (Figure 1) was constructed following the design of Huang, et. al (25). A ferromagnetic CMI-C rod (Cold Metal Products Inc) was machined and heat treated to improve its magnetic properties (25). The trap was wrapped approximately 550 times with 21 gauge copper wire which was held in place by epoxy.

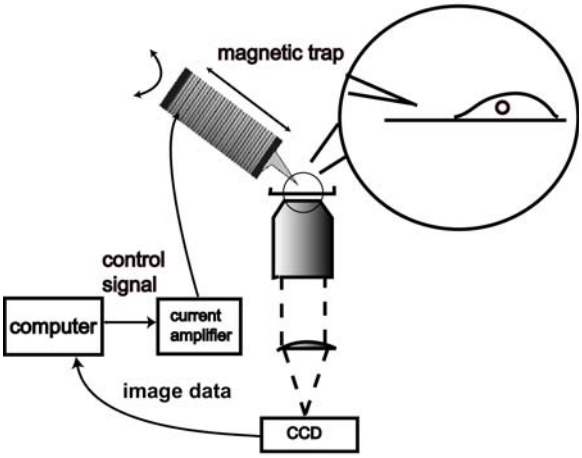

Figure 1: Magnetic trap schematic

A computer-controlled current sent through the coil generated a magnetic field that exerts force on the magnetic beads. The force increases exponentially as distance from the tip decreases (26). The displacement of the bead over time in response to a step force was recorded to determine the effective stiffness of a cell. To calibrate the trap, a force was applied to a magnetic bead in a solution of known viscosity (polydimethylsiloxane) (Sigma Aldrich, St. Louis, MO) (26). Images were recorded at 30 fps using a CMOS camera (Silicon Imaging, Costa Mesa, CA). The steady state velocity of the bead was found by measuring the displacement over time using a custom particle-tracking program (27) written in Matlab (Mathworks, Natick, MA).

For experiments in the cell, the tip of the mag-

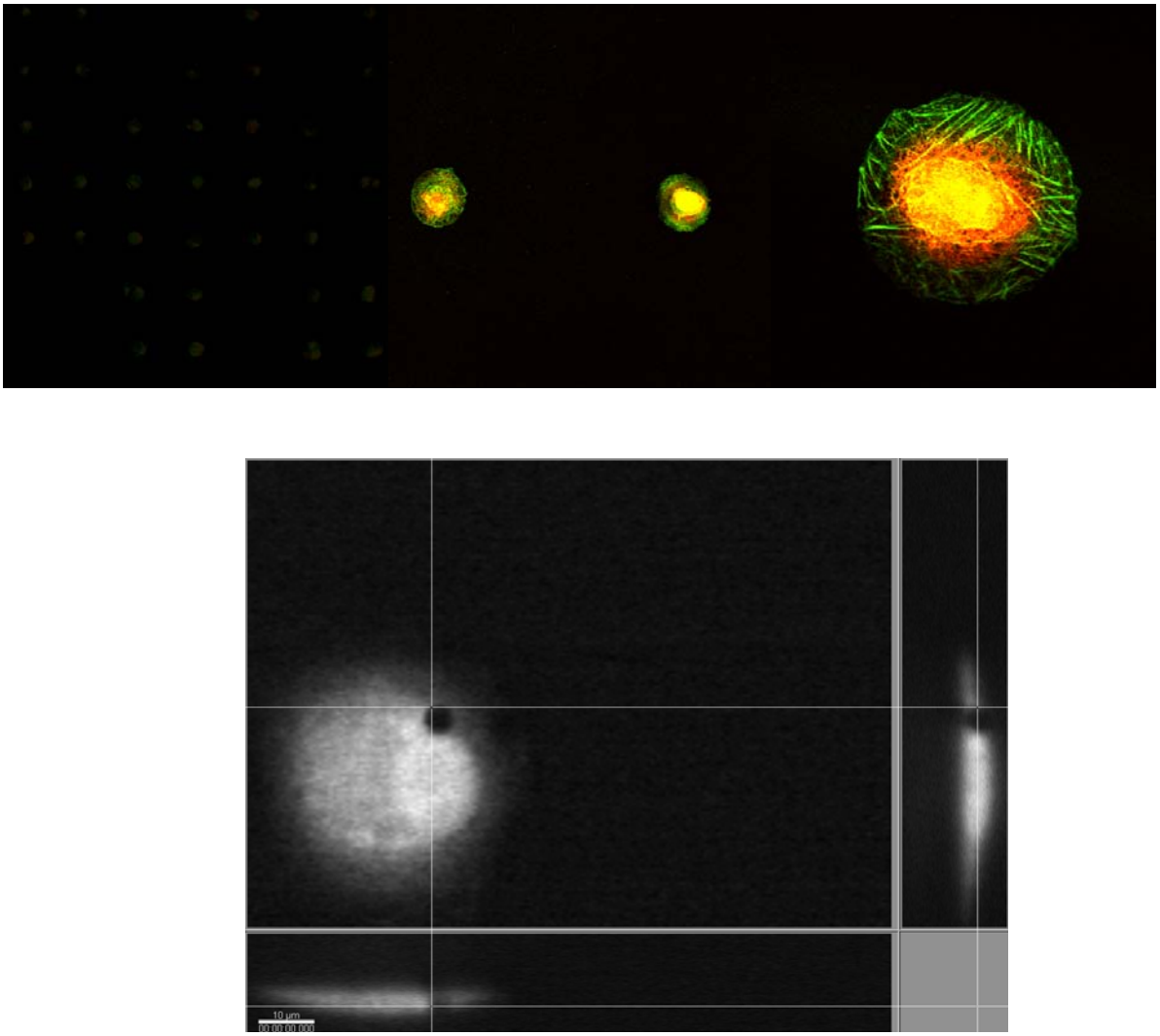

Figure 2: (top) In order from left to right: an array of 30 micron cells at 10x magnification stained with AlexaFluor488-phalloidin and Sytox Orange, two 30 micron cells at 25x magnification, and a 30 micron cell at 100x magnification. (bottom) 3D reconstruction of cell on a 50 micron pattern with an endocytosed magnetic bead. The view on the right is a section view (vertical cut) and the view on the bottom is a section view (horizontal cut). Cross hairs are located on the bead. Cells on 50 micron patterns have the lowest average height. Beads are completely internalized after 24 hours.

netic trap was wiped with 70% ethanol to prevent contamination and placed in the same plane as the bead. Cells were kept at 37 ^{o}C through the use of a temperature-controlled stage (Delta TC3, Bioptechs, Butler, PA), and an objective heater (Bioptechs, Butler, PA). For each experiment, a 5-second step-forcing function of 20 $\pm$ 1 nN of force was applied. All experiments were done at the same distance between the magnetic bead and the pole piece.

3 Results

3.1 Quantification of cellular rheological parameters as a function of area of adhesion

We used micropatterned planar circular islands of 10-, 20-, 30-, 40-, and 50- micron diameters to confine cells (Figure 2 (top)). The size range of the islands was chosen to be as wide as possible with the following consideration for the upper and lower limits: if the islands were too small ($\sim$5

microns) the cells would undergo apoptosis (14); if the islands were too large, then one single cell cannot fully spread to occupy the entire area of the island. To quantify the effective stiffness of the cells, magnetic beads were dropped on a dish of cells cultured on these substrates, allowed to internalize for 24 hours, and pulled on for 5 seconds using the step-force protocol at 20 nN amplitude as described previously. Only cells with one magnetic bead per cell were examined. The 24-hours internalization period was designed to eliminate the effect of bead rolling which occurs in beads on the cell surface because the magnetic force induces a torque around the bottom of the bead in addition to a translational movement (28). The added rotational movement of the bead causes a significant difference between the measured bead center displacement and the inferred displacement of the cell membrane thus contributing a significant error to this class of magnetic-force-based rheological measurements (28). We further found that internalized particles provided more consistent data than beads on the cell surface (where adhesion strength may vary with local receptor density). In confirmation with another published paper (29), beads were found to be internalized after 24 hours via confocal imaging (Figure 2 (bottom)).

The measured displacement of magnetic particles was fitted to a Voigt model (3) in series with a dashpot (Figure 3) to obtain the values for the three associated viscoelastic parameters that characterize the response curve. A four-parameter model consisting of a Kelvin model in series with a dashpot was also tried, but was found to be unnecessarily complicated: a three-parameter model fit the data as well as did the four-parameter model.

We can interpret the meaning of the viscoelastic parameters as follows: The free dashpot and the Voigt element experience the same force,τ, with the total deformation ε as the sum of the deformation of the Voigt element,ε_1, and the free dashpot deformation, ε_2.

From the definition of a dashpot, $D\varepsilon_2 = \frac{\tau}{\eta_2}$, where $D$is the time differential operator,τ is the force, and η_2 represents the free dashpot as

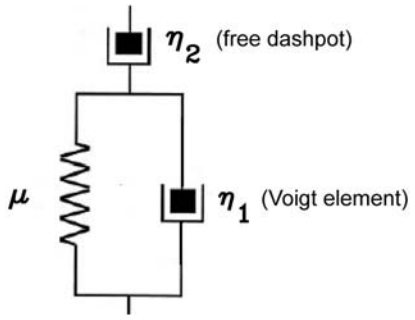

Figure 3: Voigt element in series with a free dashpot

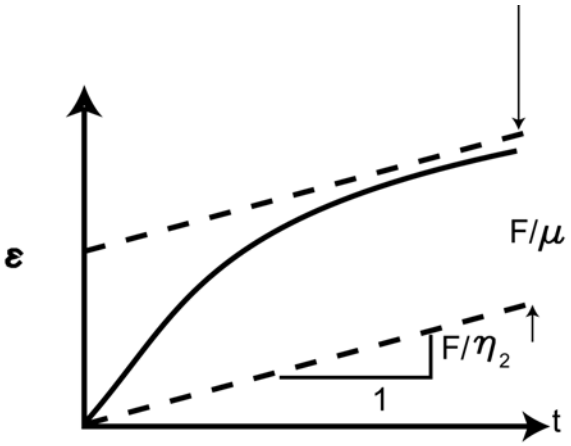

Figure 4: Response of a Voigt element in series with a dashpot for a unit step function forcing. The curve asymptotically approaches the top dashed line which represents the limiting function for large times. The lower dashed line indicates the contribution from the free dashpot.

shown in Figure 3. Therefore $\varepsilon_2 = \frac{\tau}{\eta_2 D}$ and $\varepsilon_1 = \frac{\tau}{\mu+\eta_1 D}$ Thus, $\varepsilon = \frac{\tau}{\eta_2 D} + \frac{\tau}{\mu+\eta_1 D}$ and it can then be shown that the modeling equation is: $\eta_2\mu\dot{\varepsilon} + \eta_1\eta_2\ddot{\varepsilon} = \mu\tau + (\eta_1+\eta_2)\dot{\tau}$. The solution of this equation under a step force, $F \cdot H(t)$ is: $\varepsilon(t) = F\left[\frac{t}{\eta_2} + \frac{1}{\mu}\left(1 - e^{(-t/t_\varepsilon)}\right)\right]H(t)$, where F is the force amplitude, $H(t)$, is the unit step and t_ε is the relaxation time, which equals η_1/μ. This equation is plotted as Figure 4. When the force is a rectangular function, a superposition with a time shift results in: $\tau(t) = F[H(t-t_1)] -$

$F\left[H\left(t-t_2\right)\right]$,

$$\varepsilon(t) = F\left\{\frac{t-t_1}{\eta_2} + \frac{1}{\mu}\left[1-e^{-(t-t_1)/t_\varepsilon}\right]\right\}H(t-t_1) - F\left\{\frac{t-t_2}{\eta_2} + \frac{1}{\mu}\left[1-e^{-(t-t_2)/t_\varepsilon}\right]\right\}H(t-t_2)$$

which is represented in the following plot (Figure 5):

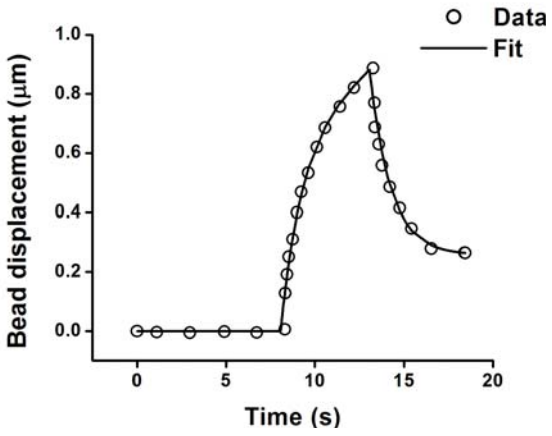

Figure 5: (top) Solution of a Voigt model in series with a dashpot for a rectangular forcing function. (bottom) Representative data and corresponding curve fit for a 30-micron diameter cell. Data points are shown at 1s intervals so that the curve fit may be seen clearly through the points.

Figure 6 shows measured values for the three viscoelastic parameters. Error bars in all of the graphs represent the standard deviation of the mean (that is, the standard deviation of the distribution divided by the square root of the number of samples).

For each cell size, the rheological response from twenty cells was analyzed. We found that the variance in the three viscoelastic parameters was significantly less than the variance in the three viscoelastic parameters obtained from the control (unpatterned cells). We noted that in the graph of η_2, due to the large difference in values between the control and patterned cells, that a different scaling was used with the break mark indicated on the vertical axis. If a uniform scale was applied, the error bars for the control would appear significantly larger than the error bars for the patterned cells. Statistical significance between values was determined by use of the Student's t-test and the (*) was used to indicate the existence of statistical significance between selected pair of measurements. It appears that μ and η_1 display a definite biphasic response as a function of pattern diameter with a minimum at 30 microns. The spring constant, μ is the measure of the elasticity and is demonstrated later to be proportional to the shear modulus, G. The values of μ and η_1 for the 20- and 30- micron diameter cells, are less than the values of these parameters for cells 10-, 40-, and 50-microns in diameter; this difference is statistically significant. We will demonstrate later that this minimum in shear modulus correlates with a minimum in the volume fraction of polymerized actin. In the graph of η_2 vs. pattern diameter (Figure 6, bottom-left), we notice that there is a significant difference between the value of the control cell and the patterned cells. The high value of η_2 of the control cell indicates that the control cell has the least residual deformation. The relaxation time,$t_\varepsilon = \eta_1/\mu$, (Figure 6, bottom-right) provides the characteristic time measure for the cell to reach its full elastic deformation; t_ε is on the order of 1 second.

We can further approximate a frequency-dependent complex shear modulus, $G^*(\omega)$, with a real part, $G'(\omega)$, and an imaginary part $G''(\omega)$, by modeling our experiments as a spherical bead embedded in a linear, infinite, uniform, and isotropic viscoelastic medium (30). Note that these validity conditions are only approximately satisfied for endocytosed particles in cells. In particular, the cell's membrane adjusts to accom-

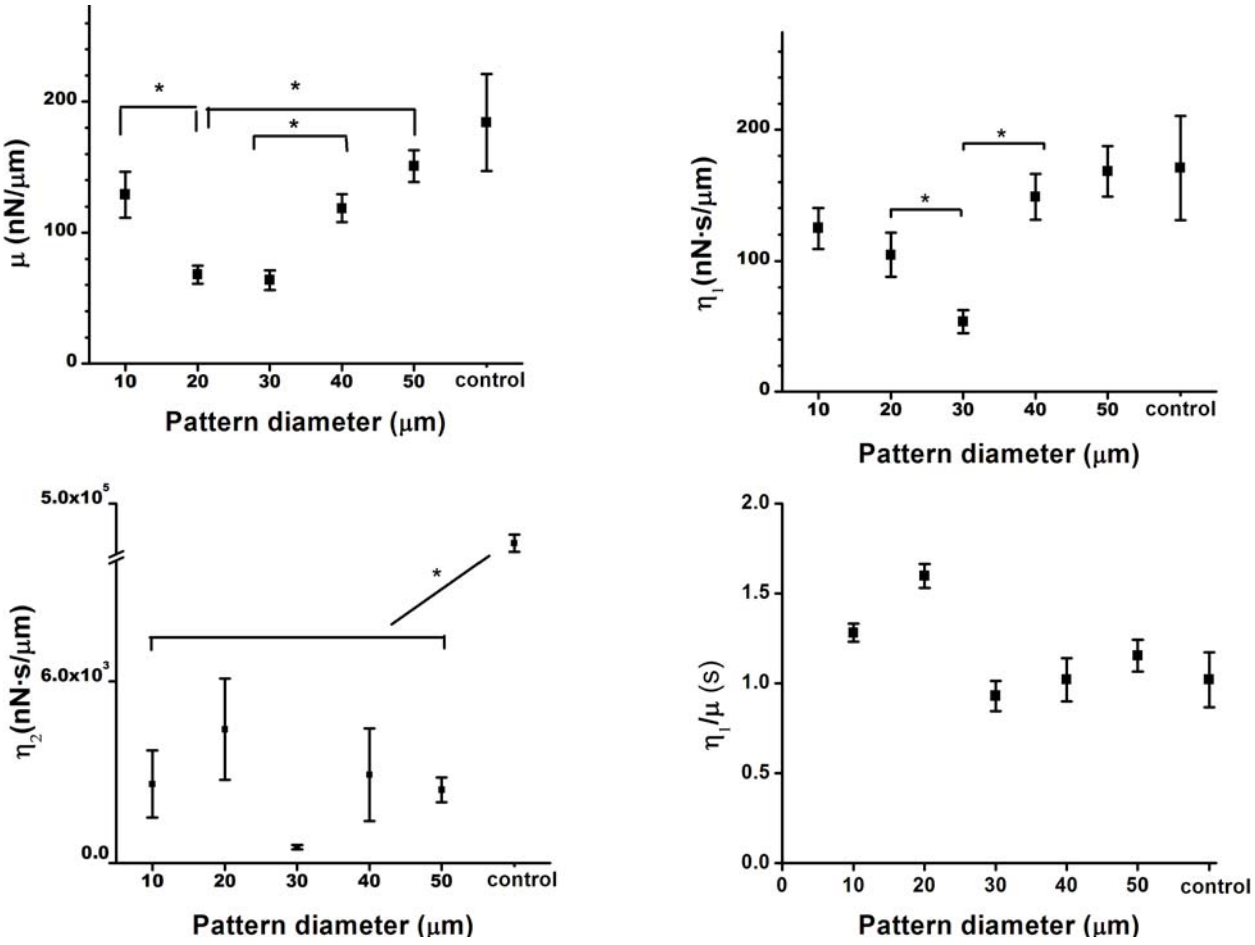

Figure 6: Viscoelastic parameters extracted from curve fit. (top-left) spring constant (top-right) dashpot in Voigt element (bottom-left) free dashpot (bottom-right) relaxation time. Twenty cells were measured for each cell size. The * above the brackets indicates statistical significance ($p < 0.05$) between values. Error bars in all graphs represent the standard deviation of the mean.

modate the height of the bead. We would like to note that despite the close presence of the cell boundary Figure 2 (bottom), these assumptions are widely assumed in all bead based rheological calculations as there exists at present no analytic expression which takes into account the boundary conditions for the calculation of the shear modulus. A versatile, precise, and efficient finite element method to account for such complicated boundary conditions has yet to be developed. As current rheological methods are unable to separate out the contributions of the membrane from the cytoskeleton, we view the shear modulus taken from this calculation as a lumped modulus which takes into account all contributions. Taking these considerations into account leads to the following established analytical expression for the complex shear modulus:

$$G^*(\omega) = \frac{f(\omega)}{6\pi R x(\omega)}$$

where $f(\omega)$ is the force exerted as a function of frequency, $x(\omega)$ is the resulting complex bead displacement, and R is the radius of the bead. We define a stiffness G to be the value of the real part of $G^*(\omega)$, $G'(\omega)$, measured at 0.05 Hz. This value was chosen to be much greater than the reciprocal of the relaxation time, $t_\varepsilon = \eta_1/\mu$. The zero frequency value, although representing the static component, was not chosen because the validity of the model breaks down due to the presence of the free dashpot which would predict infinite de-

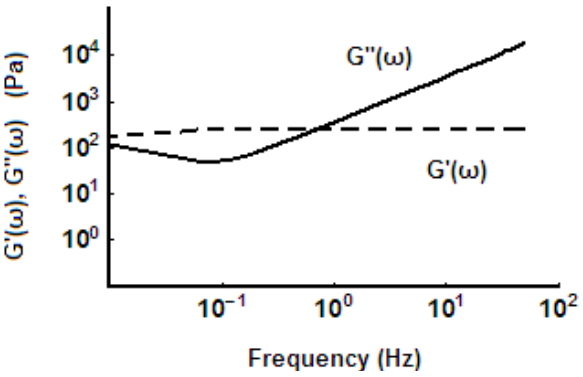

Figure 7: Representative plot of $G'(\omega)$ and $G''(\omega)$ for 30-micron diameter cell. These curves are determined analytically from curve fits of the data.

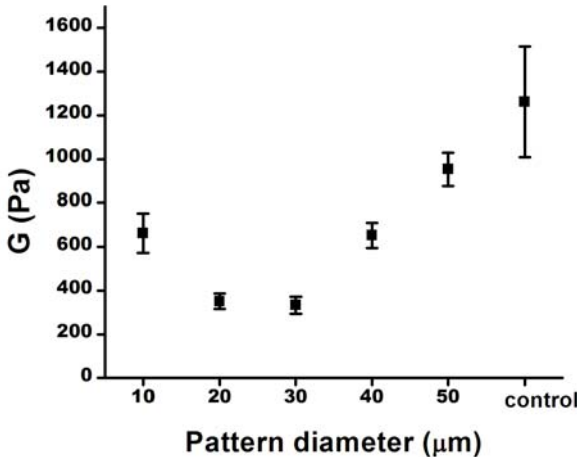

Figure 8: Shear modulus as a function of pattern diameter. Error bars represent the standard deviation of the mean (standard deviation of the distribution / square root of the number of samples).

formation at zero frequency under any force. Figure 7 shows a representative graph of $G'(\omega)$ and $G''(\omega)$ (imaginary component of $G^*(\omega)$) Figure 8 shows G as a function of pattern diameter.

Figure 8 shows a plot of G as a function of pattern diameter with error bars representing the standard deviation of the mean value. The value of G that we obtain for the control cells is on the order of 10^3 Pa; this value is within an order of magnitude of the values reported in the literature for fibroblast cells by magnetic trapping (10^4 Pa, (11)) and similar to the values reported by atomic force microscopy (10^3 Pa, (9)). It may be possible that the shear modulus for the control value is larger than any other size on the patterns due to the fact that the cell achieves maximum size if allowed to spread freely on an adhesive substrate. It is also possible that effects such as cell shape may play some role. As discussed previously, our model for $G^*(\omega)$ neglects boundary effects. One can not rule out the possibility that a change in average cell height on the different patterns can affect the accuracy of shear modulus measurement. Nonetheless, because the average cell height (total cell volume/base area) monotonically decreases while the shear modulus shows a biphasic behavior that decreases and then increases, we can conclude that while height may contribute to the uncertainty in shear modulus measurement, it is at most a secondary factor in our measurement.

The distribution of G for patterned and unpatterned cells is shown in Figure 9. We note that the shear modulus histogram for patterned cells has a much tighter distribution than the histogram for unpatterned cells. We considered several measures of variance including median absolute deviation and interquartile range (IQR). Specifically, IQR is a robust measure of spread that is designed to not be overly influenced by outliers. In both calculations, there was an increased variance of the shear modulus on the unpatterned substrates. On average, the unpatterned cells correlate with a larger area which lends credence to the notion that size rather than shape creates variability. One interpretation is that the cellular rheological properties are more homogeneous in smaller areas. When the cell gets larger, there may be regional difference accounting for the variance.

We measured the actin cytoskeleton structural parameters as a function area of adhesion (Figure 10). Polymerized actin was visualized based on phalloidin labeling. To obtain the volume of polymerized actin present in each cell, three-dimensional images of AlexaFluor488-phalloidin labeled cells confined to 10-, 20-, 30-, 40-, and 50-micron diameter circles were taken using a spinning disk confocal microscope (Perkin Elmer Ultraview, Wellesley, MA). A 100x Plan Apo

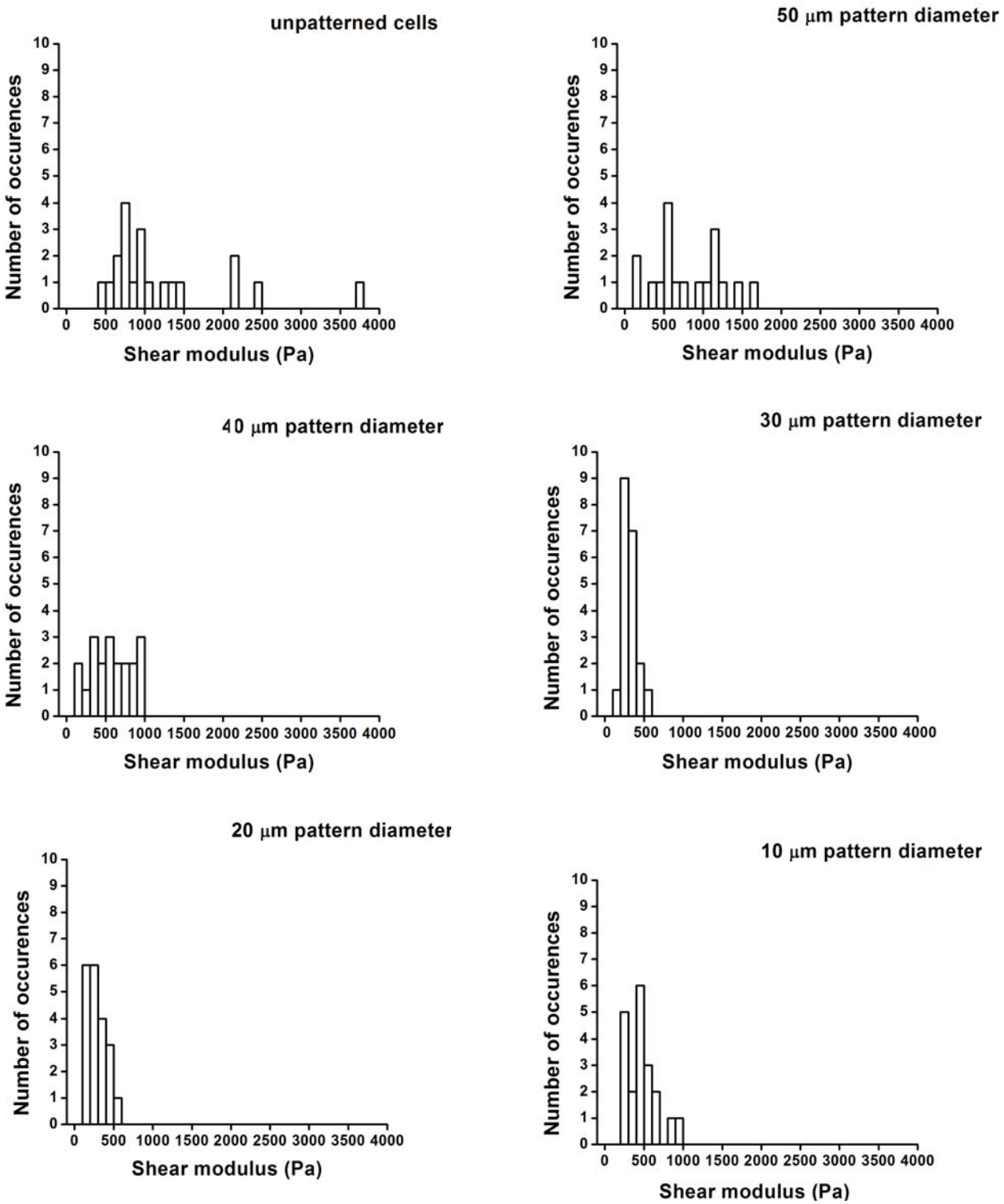

Figure 9: Distribution statistics of the shear modulus, G (value of $G'(\omega)$, measured at 0.05 Hz) for patterned and unpatterned cells.

Nikon objective with a numerical aperture of 1.45 was used for imaging. Two-dimensional slices were taken every 100 nm for a total of 1000 slices. Each three-dimensional stack was deconvolved to remove the out-of-focus light using Huygens Essential (Scientific Volume Imaging, The Netherlands) and reconstructed in the image visualization software Imaris (Bitplane AG, St. Paul, MN) where background was subtracted from the images and a consistent threshold was used to determine the presence of actin.

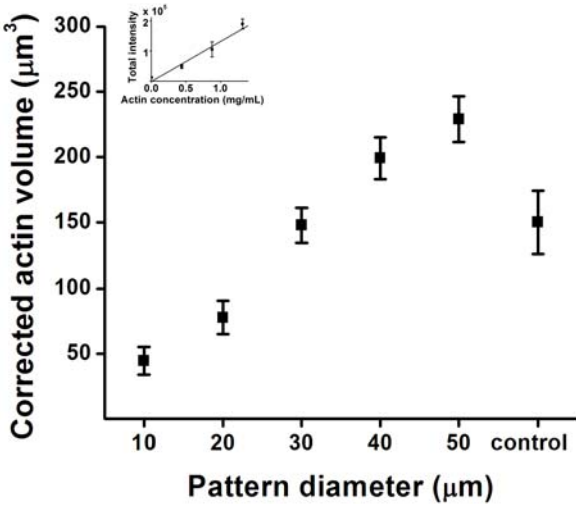

Figure 10: Corrected actin volume of the cell as a function of pattern diameter. Inset demonstrates linearity between actin concentration and total intensity. Error bars represent the standard deviation of the mean.

Because the diameter of a single actin filament (6-8 nm) is significantly less than the microscopy point spread function of about 300 nm, the measured total volume of the fluorescent voxels greatly overestimates the volume fraction of polymerized actin in the cell. However, the polymerized actin volume can be estimated using intensities by assuming that the local polymerized actin density is proportional to the bound phalloidin density and hence, to the intensity of fluorescence. The polymerized actin volume can then be determined if the fluorescence intensity emitted from a unit volume of polymerized actin can be measured. This scaling factor was obtained by imaging a gel containing similarly fluorescently labeled actin filaments at known weight concentration and measuring the corresponding intensity. Weight concentration was converted to volume concentration using the known density for actin filaments (732 mg/mL, CRC Handbook of Biochemistry). This calibration experiment provides the needed scaling factor to convert the fluorescence intensity at each voxel to the volume of polymerized actin. To further validate this approach, a series of actin-gel experiments were performed to establish linearity between actin concentration and measured fluorescence intensity (Figure 10, inset). This result is corroborated by the fact that the binding of AlexaFluor488-phalloidin and polymerized actin is stoichiometric (1:1, Molecular Probes Handbook). The proportionality of actin concentration and measured intensity is adequately verified by linear regression obtaining a reduced χ^2 value of 1.1 and a y-intercept of $0.1 \times 10^5 \pm 0.78 \times 10^3$. The corrected total actin volume of the cell linearly increases with pattern diameter and is plotted as Figure 10.

To determine the actin density as a function of pattern diameter, a measurement of the volume of the cell is needed. The total volume of each cell (Figure 11) was measured according to the conventional protocol of cell volume measurements (31) by fluorescently labeling live cells with the whole cell-permeant marker 5-chloromethylfluorescein diacetate and using confocal microscopy to image two-dimensional slices, in the present case, every 100 nm. A consistent threshold was applied to determine the extent of the cell and total volume was calculated by summing the number of fluorescent voxels (Figure 11).

The measured total cell volume (Figure 11) indicates that cell volume increases with pattern diameter and appears to approach a plateau value. The variation of total cell volume with pattern diameter deviates from the expectation that the volume would be conserved as adhesion area increases. Our cell tracker labeling result is in agreement with an independent cell volume measurement using actin labeling where a surface is numerically superimposed over the actin filament images and the volume underneath calculated (data not shown).

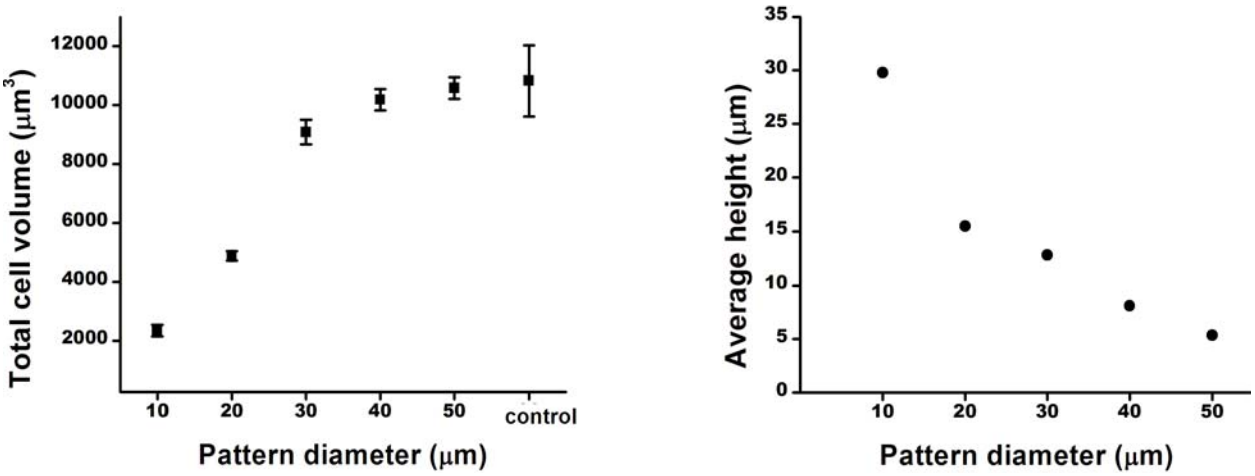

Figure 11: (left) Total cell volume as a function of pattern diameter. Error bars represent the standard deviation of the mean. (right) Average cell height as a function of pattern diameter. The height monotonically decreases whereas for the stiffness data a minimum occurs at 30 microns demonstrating that cell height is not the most critical factor in determining cell stiffness.

The ratio of the corrected actin volume to total cell volume determines the actin density or volume fraction,ϕ, of actin in each cell. (Figure 12). The value that we obtain of 1-2% is similar to the values reported for the volume fraction of endothelial cells (32).

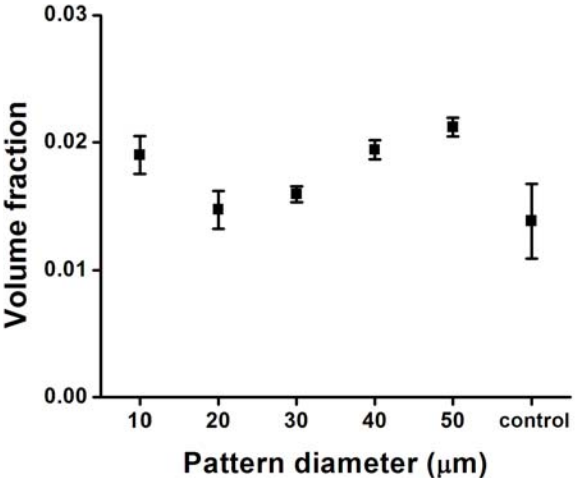

Figure 12: Volume fraction of actin as a function of pattern diameter. Error bars represent the standard deviation of the mean.

4 Discussion

The main goal of our work is to understand how cellular structural changes dictate variations in rheology. By independently measuring rheological and structural parameters as a function of adhesion area, we can relate measured rheological properties to measured cytoskeletal properties via cellular micro-mechanical models. This process also helps to evaluate the validity of these models. More specifically, we can independently predict the relative change in shear modulus obtained from magnetic trapping by substituting the volume fraction of actin present in each cell into cellular micro-mechanical models that give a scaling relation for the Young's modulus of the cytoskeletal network (based on the amount of actin present, and on its material properties) (1). These predictions provide a molecular-level explanation for the change in effective cell stiffness as measured by magnetic trapping.

Three of the best developed cellular micro-mechanical models are the tensegrity (33), cellular-solids (32), and biopolymer physics (34) model. For the tensegrity model, the structural integrity of the cytoskeleton is maintained by the interaction of elements in tension and compression. In the cellular solids theory, the cytoskeletal meshwork is treated as a compilation of staggered

unit cells connected at their midpoint by struts. In the biopolymer physics model, the cytoskeletal network is treated as a polymer gel in which there are entangled or cross-linked filaments. We emphasize the obvious: that these microstructural models are highly idealized representations of cellular structures. Nonetheless, they provide a starting point in discussions of the influence of cellular structure on cellular rheology. Although many molecular structural components, such as actin, microtubules, and intermediate filaments, can contribute to cellular rheology, we choose a simplifying assumption focusing only on the actin component of the cytoskeleton. Specifically, we have tested a simple hypothesis: changes in polymerized actin volume fraction regulate changes in cellular shear modulus. Controlling the area of cellular adhesion using microcontact printing provides a useful way to vary cellular actin volume fraction. Note that this hypothesis neglects many factors including structural contributions from other cytoskeletal components such as intermediate filaments, possible changes in actin pretension, or changes the Young's modulus of individual actin filaments. Nonetheless, as a first order hypothesis, it is reasonable to first test the role of actin density in regulating the observed cellular rheological differences.

For various formulations of the tensegrity model (e.g. two-dimensional two-strut and three-dimensional six-strut models), the network modulus,E_n, scales linearly with volume fraction (1). We fit our data into the two-strut tensegrity model, in which the Young's modulus of the network is linearly dependent on the volume fraction, ϕ, and the Young's modulus of an actin filament ($E_n \sim E_f\phi$) and the six-strut tensegrity model, in which the Young's modulus of the network scales linearly with the volume fraction of actin and the pre-stress (σ_c) and pre-strain (ε) of the network. For the theory of cellular solids, the network Young's modulus scales as $E_f\phi^2$ (29) and for the biopolymer physics model the network Young's modulus equals $k_BTl_p^2a^{-5}\phi^{5/2}$ where k_B is the Boltzmann's constant, T is temperature, l_p is the persistence length, and a is the radius of an actin filament (34). Assuming an incompressible material we can further relate the shear modulus measured experimentally with the Young's modulus, E, in the models ($E = 3G$).

Specifically, the relationship between the Young's modulus and the actin volume fraction can be expressed for all three models as follows:

$E = A\phi$ where $A \propto \frac{\sigma_c}{3}\frac{1+4\varepsilon}{1+12\varepsilon}$ for the six-strut tensegrity model

$E = A\phi^2$ where $A \propto \frac{3}{8}E_f$ for the cellular solids model

$E = A\phi^{5/2}$ where $A \propto k_BTl_p^2a^{-5}$ for the biopolymer physics model

where A is the proportionality constant encompassing factors such as pre-stress and pre-strain in the tensegrity model, the Young's modulus of actin in the cellular solids model, and temperature, persistence length, and radius of an actin filament in the biopolymer physics model. A nonlinear regression can be performed to fit our measured E as a function of ϕ by minimizing the $\chi 2$ merit function (Experimental Data Analyst, Mathematica) (Figure 13), where x_i and σ_{x_i} represent the value and the standard deviation of the mean for ϕ respectively, and σ_{E_i} is the standard deviation of the mean of the Young's modulus.

$$\chi^2(k) = \sum_{i=1}^{N} \frac{(E_i - Ax_i)^2}{\sigma_{E_i}^2 + A^2\sigma_{x_i}^2}$$

This curvefitting approach allows us to extract the proportionality constant, A, from our data. Comparing the fits of the three microstructural models, the biopolymer physics model and the cellular solids model appear to provide better agreement than the tensegrity model (Figures 13 and 14). We can analyze this in a more quantitative fashion by using a two sample independent t-test that compares the mean of all 100 observations on log E (modulus) with the mean of all 100 observations on log ϕ multiplied by the exponent of interest (1, 2, 2.5) plus the log of A. Since there are 20 observations for each pattern diameter, we weight each batch of 20 data points by our estimate of their standard error before computing the mean of all 100 points. Our probability model is that the two means are normally distributed and the difference in the means is hypothesized to be

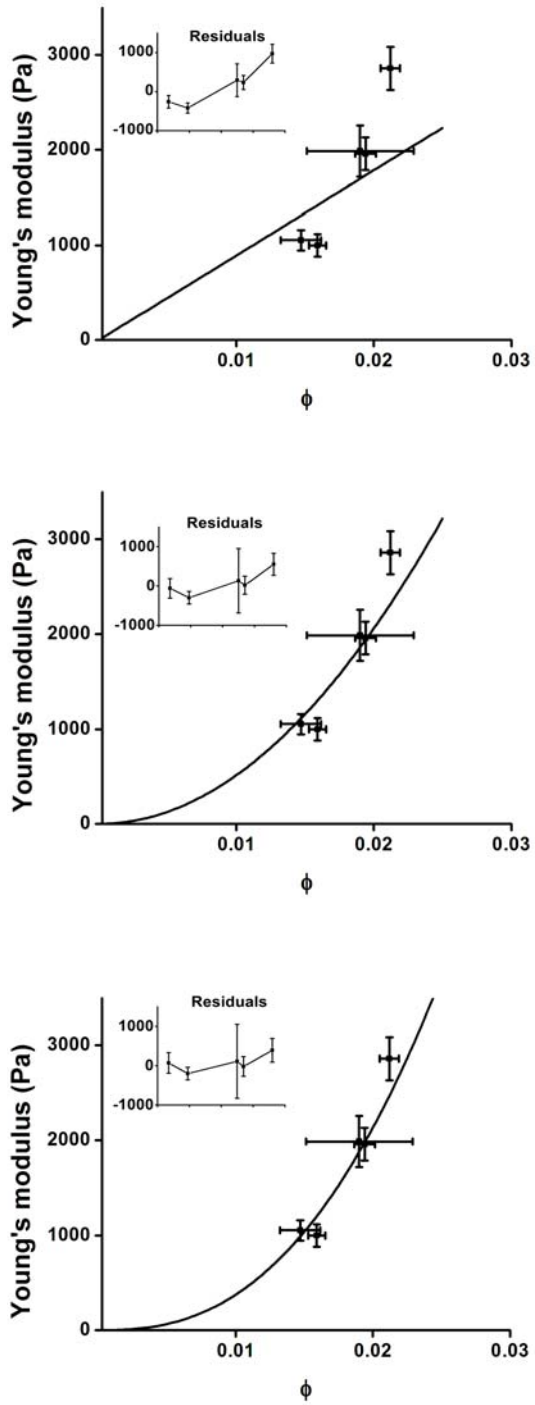

Figure 13: (top) Tensegrity model: non-linear fit of Young's modulus as a function of volume fraction, (middle) Cellular-solids model: non-linear fit of Young's modulus as a function of volume fraction squared, (bottom) Biopolymer physics model: non-linear fit of Young's modulus as a function of volume fraction to the 5/2 power. There are five data points, one for each pattern diameter.

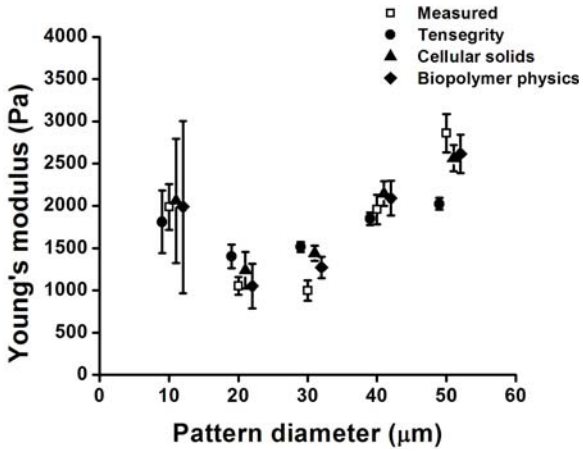

Figure 14: Young's modulus predicted by tensegrity, cellular solids, and biophysical polymer model compared to measured values. Error bars represent the standard deviation of the mean. The points are slightly separated laterally for clarity.

zero. The t-test gives a difference in the means of 2.25 for the tensegrity model, 1.91 for the cellular solids model, and 1.81 for the biopolymer physics model. At the 95% significance level the critical difference is 2 which supports our qualitative observation that the biopolymer and cellular solids models appear to provide better agreement and argues that the exponent is not correct for the tensegrity model and that it may be rejected. The error would need to be further reduced to be able to definitively distinguish between the cellular solids and biopolymer physics model.

Using the constant of proportionality, A, obtained from the linear regression, we can further calculate the Young's modulus predicted by each model using measured values of volume fraction, and compare these values to the measured Young's modulus (Figure 14).

The pre-factor, A, is an experimentally obtained scale factor associated with each model. Because these models do not predict these pre-factors a priori, the goodness of fit of the exponent of ϕ, is the only way to compare the various models. In the case of the six-strut tensegrity model, we obtain an A value of 9.16×10^4 which represents the pre-stress and pre-strain factor. This value is the same as the value calculated by Stamenovic

and Coughlin (35) for a six-strut tensegrity model. This agreement is not surprising, as the A values from both measurements were obtained by fitting the tensegrity model to experimentally measured cellular rheological data.

For the cellular solids model, the scaling pre-factor was obtained through rheological measurements of actin gels and various fibrous materials. As ϕ approaches 1, the proportionality constant represents the Young's modulus of the network. For the cellular solids model, we obtain an E_f value of 5×10^6. This value, according to the model, represents the Young's modulus of an individual strut. This value is sometimes assumed to be the Young's modulus of an individual actin filament, $E_f(10^9$ Pa, (36), (37) (38)). In actuality, however, E_f of an individual strut is unknown because the struts are most likely composed of fiber bundles which slide relative to each other and so the strut would exhibit a significantly lower modulus than that of a single filament. Further, there are many other factors such as the irregularities of the actin network which also influence the true value of the coefficient. Our value for E_f is a factor of 100 lower than the value used by Satcher and Dewey measurement (32). This difference in actin Young's modulus between our value and the Satcher and Dewey value comes from the fact that our volume fraction (which is close to 2%) is slightly higher than the volume fraction value used by Satcher and Dewey (close to 1%).

Similarly, the scaling pre-factor in the biopolymer model was also obtained through rheological measurements of actin gels. The pre-factor for biopolymer physics model that we obtain (3.7^7) is two orders of magnitude larger than the number (2×10^5) obtained from using rheological measurements of actin gels (34). The difference between these values represents differences between the bending stiffness, k_B, and the persistence length, l_p, of the filaments in the actin gel versus the cell where factors such as the degree of filament cross-linking may be different.

We can further analyze the data in a less model-dependent fashion, by fitting the data to the power law: $E = A\phi^b$. This regression (Figure 15) returns the exponent of $b = 3.48 \pm 0.02$ and using the t-test, a difference in the means of log E and log ϕ plus log A of 0.09 which suggests a different model with a steeper polymerized actin fraction dependence. A higher order ϕ dependence, with $b = 7/2$, may be obtained, for example, by modifying the biopolymer physics model. In the original biopolymer physics model, the length between entanglements,L_e, and the mesh size, ξ, are assumed to both scale with the concentration of the chains (34); however, as noted by Mackintosh, et al., the equal scaling of these quantities with concentration need not hold when $L_e \geq \xi$ (39) and may result in a greater than 5/2 dependence of modulus on ϕ.

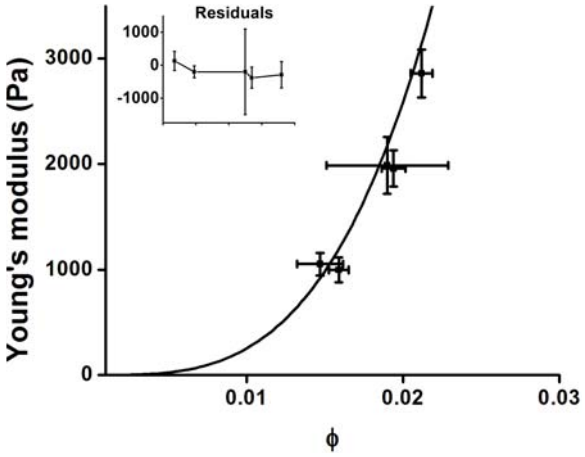

Figure 15: Fitting $E = A\phi^b$. For a pure power law model, the curve is forced to pass through the origin. There are five data points, one for each pattern diameter.

All three existing models stipulate that the curve of Young's modulus versus polymerized actin volume fraction should go through the origin; alternatively our data is consistent with the Young's modulus vanishing as the polymerized actin volume fraction goes to 0.013 ± 0.0028. This observation suggests the possibility of alternative models with a critical volume fraction,$\phi_{critical}$, of actin below which the cell will collapse on itself and have zero stiffness. Qualitatively, this model is plausible since a solid actin network requires polymerized actin fragments to reach a percolation threshold.

We consider an alternative model,$E = A(\phi -$

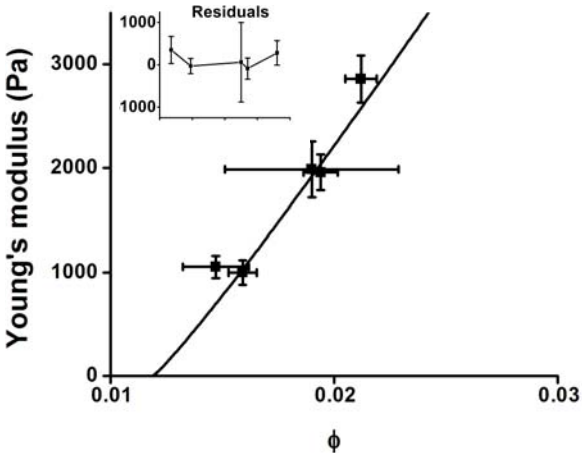

Figure 16: Modified tensegrity model fit. There are five data points, one for each pattern diameter.

$\phi_{critical})^b$, which incorporates the notion of a critical actin volume fraction (Figure 16). With this model, an exponent b = 1.0 $\pm$0.1 is obtained. Given the linear dependence of the shear modulus on polymerized actin volume fraction, this result suggests a modified tensegrity model which incorporates a critical actin volume fraction.

We can only speculate as to how cellular adhesion area affects actin density on the molecular level. A recent study by McBeath et. al., indicates that the proteins RhoA and ROCK are more active in spread than unspread cells, and that cellular shape affects cellular differentiation via RhoA and ROCK. These proteins have been established to regulate cytoskeletal tension (20) and this observation may explain the link between cellular adhesion area and cytoskeletal mechanics.

5 Conclusions

Our study has resulted in two major findings. One finding is that controlling the area of cellular adhesion reduces the variation in mechanical properties compared with unpatterned cells by a factor of approximately 4 (Figure 9). This reduction provides not only a means of engineering a cell in a specific mechanical state, but also a method of achieving higher reliability in cell mechanics measurements than has previously been possible. The large difference between the variances in the Young's modulus for the un-patterned cells and the patterned cells indicates that cell shape plays a role in determining cellular stiffness. This topic is an issue for further study. A second major finding is that adhesion area dependent changes in the shear moduli of cells that correlate with area of adhesion may be largely mediated by changes in the polymerized actin volume fraction.

In addition, although micro-mechanical models, such as the tensegrity, cellular-solids, and biopolymer physics model, have been proposed for over a decade, there is no study where model parameters are systematically varied and the predicted rheological parameters compared with experimental measurements. Soft lithography provides a powerful method with which to control cellular shear modulus and cytoskeletal structure by controlling adhesion area (and probably shape, although we have not explored this issue). This study provides the experimental data needed for critical evaluation of these three models. By relating the cellular shear modulus to the polymerized actin volume fraction, we infer that models with a higher order ϕ dependence such as the biopolymer physics model and cellular solids model, provide better agreement than the original tensegrity model. Alternatively, a modified tensegrity model with a critical actin volume fraction can provide equivalent agreement to our data.

Given that the real significance of a complex system is always less than the statistical significance since so many sources of error are omitted, neglected and underestimated, our hypothesis must be evaluated in future experiments. Specifically, measuring cellular rheology over a broader range of actin volume fractions, and examining correlations of cellular rheology with other cytoskeletal structural components, should provide valuable insight. Further, significant uncertainty in our analysis lies in the actin volume fraction measurement. This uncertainty in volume fraction partially originates from the fact that the diffusion of dye in the actin filament gel may be different than the diffusion of dye within the cell. We will account for this effect in future experiments by using stably transfected GFP-actin cells and measuring the F-actin/G-actin content using fluorescence recovery after photobleaching (FRAP),

(40). This error in the volume fraction measurement may be furthered reduced by labeling GFP-actin cells with a whole cell stain and measuring actin volume and total cell volume on the same cell.

This paper only addresses the issue of the effect of circular adhesion area on cellular mechanical properties. The investigation of axisymmetric shapes is of great interest in cell differentiation and migration. This is addressed in the companion paper.

Acknowledgements: We would like to thank Jorge Ferrer (MIT, Biological Engineering) and Alec Robertson (MIT, Mechanical Engineering) for the actin filament gels, John Wu (Harvard, Biology) for imaging Figure 2 (top), and members of the So Lab for helpful discussions. We are also grateful to Prof. Forbes Dewey (MIT, Mechanical Engineering, Biological Engineering) and Prof. Roger Kamm (MIT, Mechanical Engineering, Biological Engineering) for their comments and critical reading of the manuscript. This work was supported by NIH PO1HL64858 and a NSF graduate research fellowship (JS). The salary of Xingyu Jiang was provided by NIH GM065364.

References

1. **Stamenovic, D.; Ingber, D. E.** (2002): *Biomechan Model Mechanobiol*, 1, 95-108.
2. **Alenghat, F. J.; Ingber, D. E.** (2002): *Science's STKE*, 1-4.
3. **Fung, Y. C.** (1984): Biomechanics: Motion, Flow, Stress and Growth. Springer-Verlag.
4. **Stamenovic, D.; Fredberg, J. J.; Wang, N.; Butler, J. P.; Ingber, D. E.** (1996): *J. Theor. Biol.*, 181, 125-136.
5. **Fabry, B.; Maksym, G. N.; Butler, J. P.; Glogauer, M.; Navajas, D.; Fredberg, J. J.** (2001): *Phys Rev Lett.*, 87(14), 148102.
6. **Zahalak, G. I.; McConnaughey, W. B.; Elson, E. L.** (1990): *J. Biomech Eng.*, 112(3), 283-94.
7. **Evans, E.; Yeung, A.** (1989): *Biophysical Journal*, 56, 151-160.
8. **Yamada, S.; Wirtz, D.; and Kuo, S. C.** (2000): *Biophysical Journal*, 78(4), 1736-1747.
9. **Haga, H.; Sasaki, S.; Kawabata, K.; Ito, E.; Sambongi, T.** (2000): *Ultramicroscopy*, 82(1-4), 253-258.
10. **Choquet, D.; Felsenfeld, D. P.; Sheetz, M. P.** (1997): *Cell*, 88, 39-48.
11. **Bausch, A. R.; Möller, W.; Sackmann, E.** (1999): *Biophysical Journal*, 76, 573-579.
12. **Amblard, F.; Yurke, B.; Pargellis, A.; Leibler, S.** (1996): *Rev. Sci. Instr.*, 87, 818-827.
13. **Crick, F. H. C.; Hughes, A. F. W.** (1949): *Exp. Cell Res.*, 1, 37-80.
14. **Ziemann, F.; Radler, J.; Sackmann, E.** (1994): *Biophysical Journal*, 66, 2210-2216.
15. **Whitesides, G. M.; Jiang, X.; Ostuni, E.; Chapman, R. G.; Grunze, M.** (2004): *Polymer Preprints (American Chemical Society, Division of Polymer Chemistry)*, 45, 90-91.
16. **Jiang, X.; Whitesides, G. M.** (2003): *Eng Life Sci.*, 3, 475-480
17. **Chen, C. S; Mrksich, M.; Huang, S.; Whitesides, G. M.; Ingber, D. E.** (1997): *Science*, 276(5317), 1425-1428.
18. **Ingber, D. E.** (1993): *J. Cell Sci.*, 104, 613-637.
19. **Jiang, X.; Bruzewicz, D.; Wong, A. P.; Piel, M.; Whitesides, G. M.** (2005): *Proc. Natl. Acad. Sci. USA*, 102(4), 975-978.
20. **McBeath, R.; Pirone, D. M.; Nelson, C. M.; Bhadriraju, K.; Chen, C. S.** (2004): *Developmental Cell*, 6, 483-495.
21. **Bhatia, S. N.; Yarmush, M. L.; Toner, M.** (1998): *Journal of Biomedical Materials Research*, 34(2), 189-199.

22. **Bhadriraju, K.; Hansen, L. K.** (2002): *Experimental Cell Research*, 278, 92-100.

23. **Wang, N.; Ingber, D. E.** (1994): *Biophys J.*, 66(6), 2181-2189.

24. **Whitesides, G. M.; Ostuni, E.; Takayama, S.; Jiang, X.; Ingber, D. E.** (2001): *Annu. Rev. Biomed. Eng.*, 3, 335-373.

25. **Huang, H.** (2002): Cellular Responses to Mechanical Stresses Applied Via Magnetic Manipulators. PhD. Thesis, MIT.

26. **Su, T-T. J.** (2004): Lithographic Regulation of Cellular Mechanical Properties. MS. Thesis, MIT.

27. **Lammerding, J.; Kazarov, A. R.; Huang, H.; Lee, R. T.; Hemler, M. E.** (2003): *Proc. Natl. Acad. Sci. USA*, 100(13), 7616-7621.

28. **Karcher, H.; Lammerding, J.; Huang, H.; Lee, R. T.; Kamm, R. D.; Kaazempur-Mofrad, M.** (2003): *Biophysical Journal*, 85(5), 3336-3349.

29. **Ko, K. S.; Arora, P. D.; McCulloch, C. A. G.** (2001): *J. Biol. Chem.* 276(38), 35967-35977.

30. **Schnurr, R.; Gittes, F.; MacKintosh, F. C.; Schmidt, C. F.** (1997): *Macromolecules*, 30, 7781-7792.

31. **Sorensen, C.; Novak, I.** (2001): *J. Biol. Chem*, 276(35), 32925-32932.

32. **Satcher, R.; Dewey, C. F.** (1996): *Biophysical Journal*, 71, 109-118.

33. **Ingber, D. E.** (2003): *Proc. Natl. Acad. Sci. USA*, 100, 1472-1474.

34. **Mackintosh F. C.; Kas, J.; Janmey, P. A.** (1995): *Physics Review Letters*, 75(4), 4425-4428.

35. **Stamenovic, D.; Coughlin, M. F.** (1999): *J. Theor Biol.*, 201, 63-74.

36. **Higuchi, H.; Yanagida, T.; Goldman, Y. E.** (1995): *Biophysical Journal*, 69, 1000-1010.

37. **Tsuda, Y.; Yasutake, H.; Ishijima, A.; Yanagida, T.** (1996): *Proc. Natl. Acad. Sci. USA*, 93, 12937-12942.

38. **Yasuda, R.; Miyata, H.; Kinosita, K.** (1996): *J. Mol Biol.*, 263, 227-236.

39. **Colby, R. H.; Rubinstein, M.** (1991): *Macromolecules*, 25, 996-998.

40. **McGrath J. L.; Tardy, Y.; Dewey, C. F.; Meister, J. J.; Hartwig, J. H.** (1998): *Biophysical Journal*, 75(4), 2070-2078.